



Tuning octahedron sites in MnFe_2O_4 spinel by boron doping for highly efficient seawater splitting

Meng Chen^a, Nutthaphak Kitiphatpiboon^a, Changrui Feng^a, Qiang Zhao^d, Abuliti Abudula^a, Yufei Ma^{c,*}, Kai Yan^{e,*}, Guoqing Guan^{a,b,**}

^a Graduate School of Science and Technology, Hirosaki University, 1-Bunkyocho, Hirosaki 036-8560, Japan

^b Energy Conversion Engineering Laboratory, Institute of Regional Innovation (IRI), Hirosaki University, 3-Bunkyocho, Hirosaki 036-8561, Japan

^c College of Chemistry and Materials Science, Hebei Normal University, Shijiazhuang 050025, Hebei China

^d School of Chemistry and Environmental Engineering, Shanxi Datong University, Datong 037009, China

^e School of Environmental Science and Engineering, Sun Yat-sen University, Guangzhou 510275, China

ARTICLE INFO

Keywords:

Seawater splitting
 MnFe_2O_4 spinel
 Boron doping
 Oxygen evolution reaction
 Intrinsic activity
 Stability

ABSTRACT

Seawater splitting requires highly active and stable electrocatalysts to sustain electrolysis without chloride corrosion, especially for the anode. Herein, a boron (B) doped MnFe_2O_4 spinel-type electrocatalyst with a heterostructure was derived from MnFe-MOF-74 precursor and applied for seawater electrolysis. It is found that the introduction of B species can effectively optimize the electronic configuration of MnFe_2O_4 with the promoted electron transfer ability between neighboring O to Fe_{OH} , thereby significantly reducing the energy barrier of the electron transfer and boosting the reaction process. As expected, in the real seawater environment, it required a low overpotential of 330 mV for oxygen evolution reaction (OER) to drive a current density of 100 mA cm^{-2} at 60°C , and exhibited high stability for over 200-h continuing test without producing hypochlorite and corrosion. This work provides a new strategy for enhancing the intrinsic activity of spinel-type oxides in seawater splitting.

1. Introduction

Water splitting with renewable energy such as wind and solar power as well as surplus electricity for hydrogen production should be a sustainable technology to decrease the demand of fossil fuels and solve environmental pollution issues in the future [1–3]. In the overall water splitting process, oxygen evolution reaction (OER) at anode is a four-electron transferring reaction with a sluggish and multi-step proton-coupled process, which will impact the splitting energy efficiency [4–6]. On the other hand, considering the growing population and intensified water pollution, fresh water is becoming the limited resource around the world. Fortunately, seawater covers 71 % of the earth surface and represents ca. 97 % of water resources in the world, which is deemed as an inexhaustible resource for hydrogen production [7–9]. Combining seawater splitting with those ocean energies such as wave, wind and solar energy could realize the goal of producing clean and sustainable hydrogen energy. While, the use of hydrogen can generate pure fresh water for our daily life, which is significant to the creating of a

sustainable society, especially for the coastal and arid areas. Therefore, seawater should be considered as an ideal feedstock for electrocatalytic hydrogen production. However, one critical challenge in the direct seawater splitting is to solve the issues relating to high content of chlorine anions (Cl^-), including the chlorine evolution reaction (CER) at a low pH situation and chlorine oxidation reaction to generate hypochlorite at a high pH condition [10,11]. Compared with the acid or neutral solution, the alkaline water splitting could provide a larger overpotential (η) window limit for OER selectivity. In the alkaline condition, it is found that the highly catalytically active catalysts with OER overpotential less than 480 mV especially at high current densities are more favorable to avoid the formation of hypochlorite, where the best probability to achieve 100 % Faradaic efficiency of O_2 generation could be realized [12,13]. The other critical challenge is the very complex composition of natural seawater, in which various dissolved ions such as Ca^{2+} , and Mg^{2+} and the bacteria/ microbes and small particles could poison and pollute the electrodes and decay the catalytic performance [13,14].

* Corresponding authors.

** Corresponding author at: Energy Conversion Engineering Laboratory, Institute of Regional Innovation (IRI), Hirosaki University, 3-Bunkyocho, Hirosaki 036-8561, Japan.

E-mail addresses: yufeima@gdut.edu.cn (Y. Ma), yank9@mail.sysu.edu.cn (K. Yan), guan@hirosaki-u.ac.jp (G. Guan).

<https://doi.org/10.1016/j.apcatb.2023.122577>

Received 22 December 2022; Received in revised form 2 March 2023; Accepted 3 March 2023

Available online 5 March 2023

0926-3373/© 2023 Elsevier B.V. All rights reserved.

Numerous studies have been dedicated to exploring efficient OER catalysts for seawater splitting. Among them, transition metal oxides (MO_x , $\text{M}=\text{Fe}$, Co , Mn , Ni , etc.) hold promising merits with various nanostructures, which are suitable for catalysis process and have high resistance to corrosion [15–17]. In particular, spinel-type metal oxides (AB_2O_4 , A , $\text{B}=\text{transition metal}$) have been considered as the promising substitute for the noble-metal based catalysts due to their high intrinsic OER activities and tunable chemical composition features [18,19]. For the normal spinel, the cation A charged as $+2$ occupies the center of the tetrahedrally coordinated position while the cation B charged as $+3$ occupies the octahedral position, and the O^{2-} locates at the polyhedral vertexes [20,21]. From the study by Wei and co-workers [22], the metal cations occupied on the octahedral sites play an efficient role in the OER process due to the large overlap of the lying e_g -3d orbital in the octahedrally coordinated metal cations with an orbital of $\text{O } 2p$. Hence, further shifting the charge to those catalytically critical octahedral sites is essential in boosting OER activity. It is found that non-metal element (e.g., P, F or B) doping is a facile and efficient method for the reconfiguring of the desired surface of spinel for improving OER activity in both alkaline fresh water and seawater media [23,24]. Especially, the incorporation of the electronegative boron (B) into oxides could reduce the oxidation reaction barrier under an applied bias and facilitate the charge transfer [25]. For example, Yu et al. [26] found that coupling of B in cobalt spinel oxide could tune the surface structure to boost OER activity.

MnFe_2O_4 has a unique structure, in which the oxygen atoms constitute a face-centered cubic close-packed structure with multiple distributions of Fe and Mn cations. It is reported that the octahedral Fe sites can easily split water molecule to provide intermediates whereas the Mn-based oxides always present outstanding OER selectivity in the seawater splitting due to the weak chlorine ion adsorption on them by surface polarization [23,27,28]. Thence, in this study, a FeMn bimetal-based nanocrystalline MnFe_2O_4 spinel doping with B ($\text{B-MnFe}_2\text{O}_4$) prepared under ambient condition was considered as the OER electrocatalysts for seawater splitting for the first time. Using in situ conversion of MnFe-MOF-74 precursor coated on nickel foam (NF) by calcination in air followed with alkaline NaBH_4 solution treatment, ultrathin B-MnFe $_2\text{O}_4$ nanosheets were formed on amorphous nanowires composed of Mn, Fe, O and C species (denoted as MFOC hereafter). Furthermore, by using XPS analysis and DFT calculations, it is confirmed that the B-engineering of MnFe_2O_4 can configure the electronic structure, reduce the free energy and promote the OER kinetics. It is expected that such a unique hierarchically-architected B-MnFe $_2\text{O}_4$ @MFOC composite could provide abundant active sites, high conductivity and corrosion-resistance in the seawater splitting.

2. Experimental

2.1. Chemicals and materials

2,5-dihydroxyterephthalic acid (DHTA, 98 %) was purchased from TCL, Japan. Iron (II) sulfate heptahydrate ($\text{FeSO}_4 \cdot 7 \text{H}_2\text{O}$, 98 %), manganese (II) sulfate monohydrate ($\text{MnSO}_4 \cdot \text{H}_2\text{O}$, 97 %), N, N-dimethylformamide (DMF, deoxidized), sodium borohydride powder (NaBH_4 , powder, 95%), hydrochloric acid (HCl, 69 %), potassium hydroxide (KOH, 85 %), sodium chloride (NaCl, 99 %) were provided from Wako, Japan. Ethanol ($\text{C}_2\text{H}_5\text{OH}$, 99.5 %) and deionized (DI) water (18.2 $\text{M}\Omega \cdot \text{cm}$ @ 25 °C) were used to wash the sample. NF (thickness: 1.5 mm; number of pores per inch: 110; bulk density: 0.23 g/cm^3) was purchased from MTI, Japan.

2.2. Synthesis of MnFe-MOF-74 precursor

A piece of NF with a surface area of $2 \times 2 \text{ cm}^2$ was ultrasonicated in 3 M HCl solution, ethanol and DI water for one hour, respectively, and then heated at 60 °C overnight in a vacuum state. In a typical MnFe-

MOF-74 precursor synthesis process, 48 mg of DHTA, 78 mg of $\text{FeSO}_4 \cdot 7 \text{H}_2\text{O}$ and 13 mg of $\text{MnSO}_4 \cdot \text{H}_2\text{O}$ were dissolved in 25 mL of DMF with stirring for 3 h followed with sonicating for 1 h. Thereafter, a piece of the treated NF was immersed into a 50 mL Teflon-lined stainless-steel autoclave containing the above solution, following by a 20-h thermal treatment at 140 °C. After the autoclave was cooled down to room temperature naturally, the MnFe-MOF-74 precursor coated NF was rinsed with ethanol before heated at 60 °C overnight in a vacuum state.

2.3. Synthesis of MFOC nanowires

MnFe-MOF-74 precursor coated NF was calcined in a Muffle furnace at 250 °C for 2 h with a heating rate of 1 °C min^{-1} under air atmosphere. After naturally cooled down to room temperature, the amorphous nanowires (composed of Mn, Fe, O and C species, denoted as MFOC) coated NF electrode was obtained.

2.4. Synthesis of B-MnFe $_2\text{O}_4$ @MFOC

The as-prepared amorphous MFOC nanowires coated NF electrode was further treated by a freshly prepared alkaline NaBH_4 solution (1 M NaBH_4 dissolved in 0.1 M NaOH solution) for 20 min at room temperature. Then, the electrode was washed repeatedly with DI water to completely remove those residual ions, and finally vacuum-dried at 60 °C for 12 h. Based on inductively coupled plasma mass spectrometry (ICP-MS-7700) analysis and various preliminary investigations, the optimal element mass amounts in the electrocatalyst were found to be $\sim 0.17 \text{ mg cm}^{-2}$ for Fe, $\sim 0.03 \text{ mg cm}^{-2}$ for Mn and $\sim 0.002 \text{ mg cm}^{-2}$ for B element in this study.

2.5. Synthesis of B-Fe $_3\text{O}_4$ @FOC and B-Mn $_3\text{O}_4$ @MOC

The B-Fe $_3\text{O}_4$ @FOC (FOC: amorphous material composed of Fe, O and C species) and B-Mn $_3\text{O}_4$ @MOC (MOC: amorphous material composed of Mn, O and C species) were also prepared with the same method as that of B-MnFe $_2\text{O}_4$ @MFOC but without the addition of the precursor containing Mn or Fe element.

2.6. Synthesis of standard MnFe $_2\text{O}_4$ spinel

10 mL of mixed metallic salt solution with a Fe(III)/Mn(II) molar ratio of 2:1 were stirred and the pH was adjusted to 12 by NaOH. Then, the solution with a piece of treated NF was added into a 50 mL Teflon-lined stainless-steel autoclave and heated at 200 °C for 12 h. After the product was washed for several times with DI water and ethanol successively, the MnFe $_2\text{O}_4$ spinel coated NF electrode was obtained after heated at 60 °C overnight in a vacuum state.

Electrochemical investigation methods, catalysts characterizations and the methods on density functional theory (DFT) calculation can be found in [Supplementary Materials](#).

3. Results and discussion

As illustrated in Fig. 1, the fabrication of B-MnFe $_2\text{O}_4$ @MFOC composite-coated NF electrode mainly contains three steps. First, the MnFe-MOF-74 precursor is coated on NF by using a solvothermal method with the dissolved Fe, Mn salts and organic linkers in the DMF solution. Subsequently, by annealing MnFe-MOF-74 nanowires precursor coated NF at 250 °C for two hours, the amorphous MnFeOC compound coated electrode is obtained. Finally, the B-MnFe $_2\text{O}_4$ @ MFOC coated on NF electrode is prepared by using NaBH_4 as the reductant as well as boron source at the ambient temperature. Herein, the H^- originated from NaBH_4 has a strong reducing ability, which also serves as the oxygen scavenger to generate oxygen defects and simultaneously change the crystallinity of sample [29]. Moreover, during the reducing process, lattice reconstruction of the randomly arranged structural units in

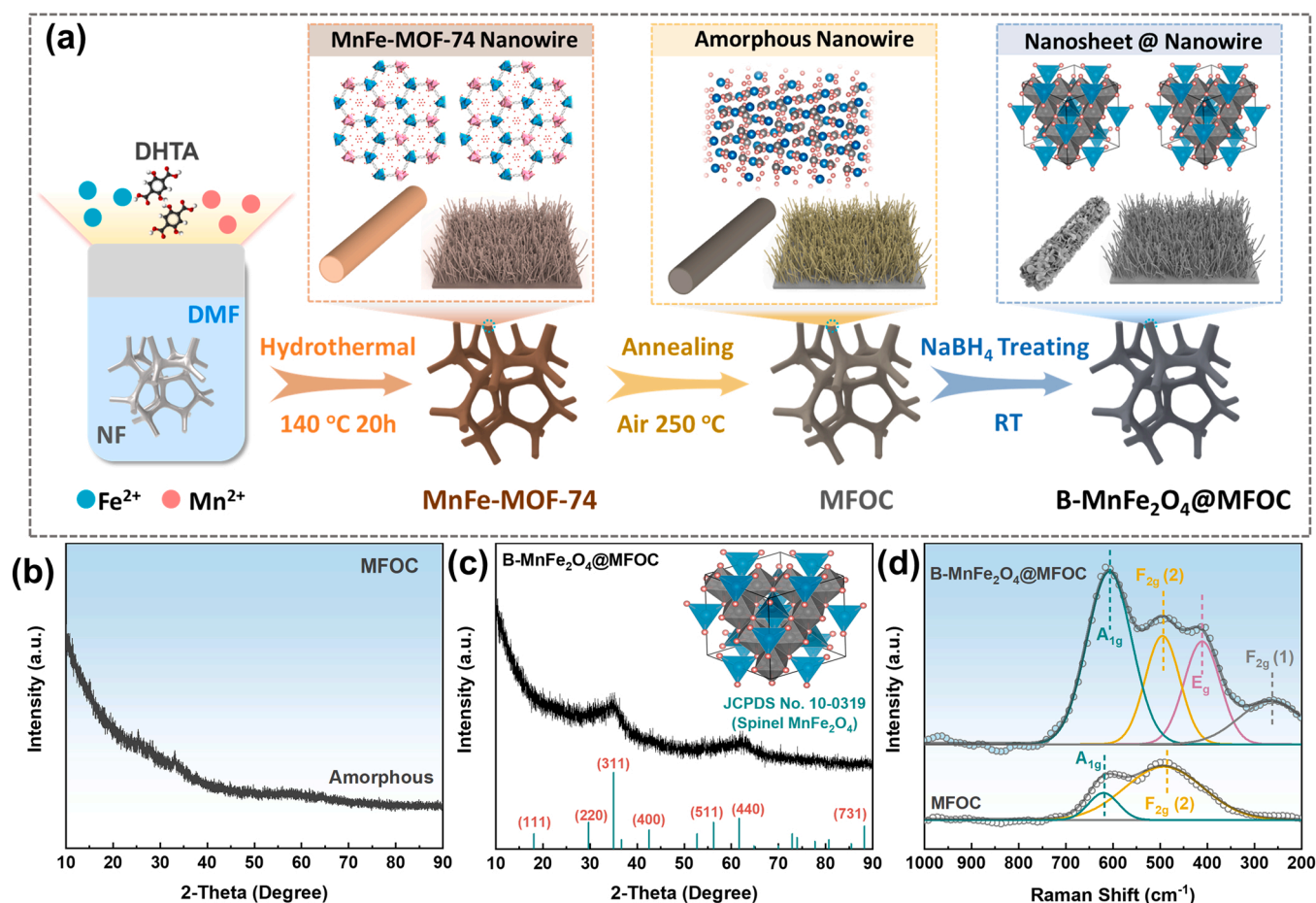


Fig. 1. (a) Schematic illustration of the preparation of B-MnFe₂O₄ @MFOC coated NF electrode; (b) XRD pattern of MFOC; (c) XRD pattern of B-MnFe₂O₄ @MFOC and (d) Raman spectra of MFOC and B-MnFe₂O₄ @MFOC.

amorphous MFOC also occurs, resulting in the transformation of amorphous MFOC into crystalline MnFe₂O₄ spinel owing to its lower activation energy barrier [30]. In addition, some oxygen species of MnFe₂O₄ spinel could be replaced by B species, leading to B doping in the spinel framework. The existence of amorphous MFOC layer between B-MnFe₂O₄ spinel and NF surface is expected to facilitate the interfacial contact and solid-state diffusion due to the short diffusion distance as well as the large surface area. Fig. S1 shows the optical photographs of different materials coated on NF substrate. In the macroscopic scale, the color of NF is changed from silver gray to black for the coating of FeMn-MOF-74 precursor on the NF, reddish-brown color for the MFOC generation, and dark brown color after the formation of B-MnFe₂O₄ on MFOC.

X-ray diffraction (XRD) patterns of all obtained precursors (Fig. S2) have two well-defined and strong diffraction peaks at 2θ between 6° and 15° , which are consistent with the (110) and (300) planes of simulated MOF-74 crystalline structure, indicating the successful syntheses of Mn-MOF-74, Fe-MOF-74 and Mn-Fe-MOF-74 on the NF substrate [31]. The different peak intensities also prove the successful doping of Mn and Fe elements into the MOF-74 framework successfully. However, no evident characteristic peaks of the MOF-74 phase are observed in the XRD pattern of MFOC (Fig. 1b), indicating its amorphous structural feature. Fig. 1c displays XRD pattern of the final as-prepared B-MnFe₂O₄ @MFOC, confirming the formation of MnFe₂O₄ spinel phase (JCPDS, No. 10-0319) on MFOC. Additionally, the broadened XRD peaks indicate that the obtained materials have a nanoscale grain size. The same phenomena are also observed from the XRD patterns of B-Fe₃O₄ @FOC (FOC: Fe-O-C compound) and B-Mn₃O₄ @MOC (MOC: Mn-O-C compound), as shown in Fig. S3. Raman spectroscopy is also used to

investigate the crystallographic phase as well as local cation distributions in details. In the ferrite spinel material, the electron transport property usually depends on the cation distribution in the tetrahedral (A-site) and octahedral (B-site) sites [32]. According to the factor group analysis, the MnFe₂O₄ spinel shows four Raman active modes, in which those of A_{1g}, F_{2g}(2) and F_{2g}(1) belong to the tetrahedral A-sites while E_g is related to the octahedral B-sites. Fig. 1d shows the Raman spectroscopy of B-MnFe₂O₄ @MFOC and MFOC. Compared to a flat curve of MFOC, four Raman modes of B-MnFe₂O₄ @MFOC are observed at 607, 495, 410 and 265 cm⁻¹ (summarized in Table S1), which are attributed to A_{1g}, F_{2g}(2), E_g and F_{2g}(1), respectively, indicating that the observed Raman bands are well matched with those of the normal spinel MnFe₂O₄ structure [32,33]. It is further proved that the MnFe₂O₄ structure has been prepared successfully. Fig. S4 shows the thermal behaviors of MFOC and B-MnFe₂O₄ @MFOC samples. The main weight loss region of B-MnFe₂O₄ @MFOC is identified in the temperature ranged from room temperature to 550 °C whereas the weight of MFOC is decreased continuously with the increase in the temperature. This may be due to that the catalyst surface structure has changed after the chemical reduction by NaBH₄. From SEM images, one can see that bulk Mn-MOF-74 particles (Fig. S5b) exist on the NF surface (Fig. S5a). In comparison, Fe-MOF-74 (Fig. S5c) and MnFe-MOF-74 (Fig. S5d) formed on NF are needle-like nanowires with sharp tips. The magnified image of MnFe-MOF-74 (Fig. 2a) reveals that the nanowires have a uniform size with an average diameter of ~150 nm and lengths up to several microns. After annealing in the air, the morphology of MFOC has no obvious change (Fig. 2b). The well-separately grown MFOC nanowires with large open spaces on NF are observed, which could act as the perfect conductive platform for guiding the growth of B-MnFe₂O₄ nanosheets in

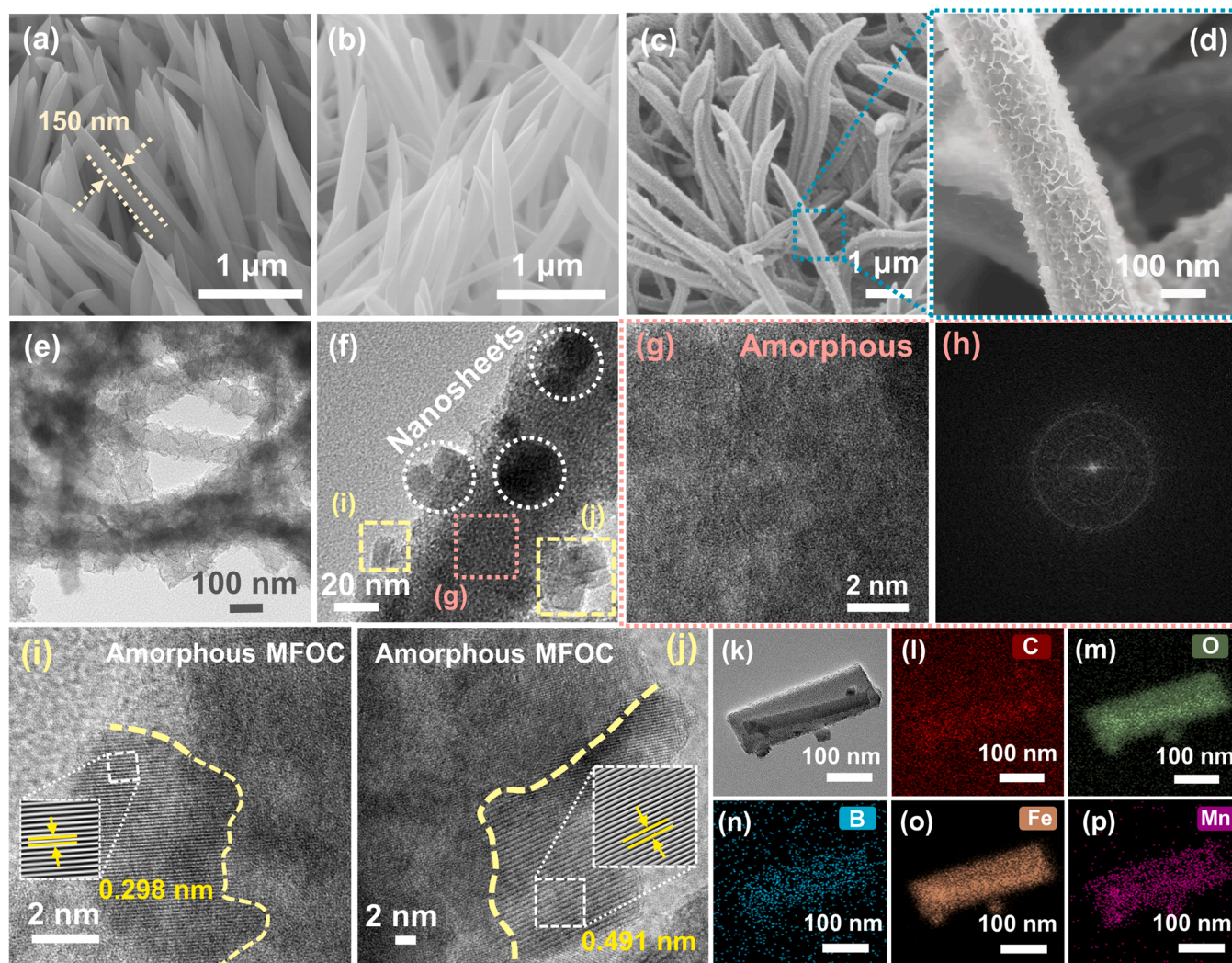


Fig. 2. SEM images of (a) MnFe-MOF precursor; (b) MFOC and (c-d) B-MnFe₂O₄ @MFOC on the NF; (e) TEM images of B-MnFe₂O₄ @MFOC; (f) HR-TEM image showing nanosheet@nanowire heterostructure, in which the nanosheets are marked by white dashed curves; (g) enlarged HRTEM image of the pink dashed square in (f) image; (h) corresponding FFT pattern of the (g) image; (i-j) enlarged HRTEM images of the yellow dashed square in (f) image; (k-p) TEM-EDS mappings of B-MnFe₂O₄ @MFOC.

the next step, leading to a large increase of effective surface area. As shown in Fig. 2c and d, the nanowire-state MFOC has been changed to a nanosheet@nanowire heterostructure (i.e., B-MnFe₂O₄ @MFOC) with a uniform core@shell nanostructure after the chemical reduction by alkaline NaBH₄ solution. That is, the surface of the MFOC nanowire is covered by interconnected ultrathin B-MnFe₂O₄ nanosheets. Herein, the generated loose porous structure with plentiful free spaces should facilitate the electrolyte infiltration, especially ion diffusion in the electrode, and generated gases releasing [34]. To further prove the role of nanosheet@nanowire heterostructure in the OER process, the contact angles of water on the surfaces of MFOC and B-MnFe₂O₄ @MFOC were measured (Fig. S6). Compared with the water contact angle on the surface of MFOC (38°), the average water contact angle on the surface of B-MnFe₂O₄ @MFOC was significantly reduced to 0°, even barely undetected, suggesting that the surface of B-MnFe₂O₄ @MFOC has excellent hydrophilicity, which should be more favorable for the aqueous electrolyte solution to well contact with the electrocatalyst, conducting to the adsorption of water molecules and fast ionic diffusion and finally improving the catalysis performance. EDS analysis (Fig. S7g) indicates the existence of C, O, B, Fe, Mn elements, and all of them distribute uniformly on the B-MnFe₂O₄ @MFOC. Interestingly, when the NaBH₄ reduction time is reduced to 10 min, it can be observed that few

nanosheets are grown (Fig. S8a and b); however, the nanosheets are replaced by nanoparticles grown on the MFOC (Fig. S8c and d) when the reduction duration for the formation of the B-MnFe₂O₄ shell is increased from 20 to 40 min. Therefore, the 20-min should be the optimal treatment time since the excessive reduction leads to agglomeration, reducing the number of active sites and surface area. As displayed in Figs. S9 and S10, the nanosheet-state B-Fe₃O₄ and B-Mn₃O₄ are also grown on the FOC and MOC respectively after the reduction by NaBH₄ for 20 min.

The B-MnFe₂O₄ @MFOC was stripped from NF for TEM and HR-TEM observations to obtain the detailed nano-scale morphological and heterointerface information. As illustrated in Fig. 2e and f, the MFOC wire is clearly wrapped by a layer of B-MnFe₂O₄ nanosheets to form a core@shell nanostructure, which is consistent with the SEM observation. Noticeably, the inner core material presents an amorphous area (selected with pink square, Fig. 2g), which is further identified by the corresponding diffraction ring (Fig. 2h) with the fast Fourier transform (FFT) pattern. It is also confirmed by the TEM images of MFOC in Fig. S11, in which the selected areas have only weak reflection halos in the diffraction pattern of MFOC sample, demonstrating the amorphous state of nanowire. While, an interface between B-MnFe₂O₄ and MFOC is clearly observed in Fig. 2i and j. In addition, the B-MnFe₂O₄ nanosheets

based shell structure reveals a polycrystalline nature, where the fringe lattice spacings of 0.298 and 0.491 nm can be indexed to the characteristic (220) and (111) planes of the MnFe_2O_4 nanocrystal, respectively, indicating that the nanosheets are composed by the crystalline MnFe_2O_4 . For comparison, the HR-TEM images of Fe_3O_4 @FOC and Mn_3O_4 @MOC are also shown in Figs. S12 and S13, respectively, in which the interplanar spacings of 0.259 and 0.297 nm are matched well with the (311) and (220) planes of Fe_3O_4 and Mn_3O_4 , respectively. Besides, EDS analysis results confirm the existence of element B within the resultant B- MnFe_2O_4 @MFOC (Fig. S14). Meanwhile, like the elemental mapping of MFOC (Fig. S15), the B, C, O, Fe and Mn elements are also uniformly distributed on the nanowire (Fig. 2k-p).

Fig. 3a shows the wide-scan XPS profiles of the synthesized electrocatalysts, in which Fe 2p, Mn 2p, C 1s, O 1s and B 1s are found at 710, 640, 285, 532 and 190 eV, respectively, also indicating the existence of B besides Fe, Mn, C and O on the surface of B- MnFe_2O_4 @MFOC (the details on the elemental contents are summarized in Table S2). In the Fe 2p high-resolution XPS spectrum of B- MnFe_2O_4 @MFOC (Fig. 3b), two spin-orbit doublets at binding energies at ca. 711 and 725 eV can be attributed to the Fe $2p_{3/2}$ and Fe $2p_{1/2}$, respectively. Furthermore, the profile of the Fe $2p_{3/2}$ spectrum can be deconvoluted into four peaks, suggesting four states of Fe species on the surface, where the bonding energies at 710.54, 712.35 and 714.33 eV assign to Fe^{2+} , Fe^{3+} (in spinel octahedron site, Oh) and Fe^{3+} (in spinel tetrahedron site, Td), respectively [35]. It should be noted that an additional peak of Fe-B at ~ 707 eV is fitted in the high-resolution XPS spectra of Fe, and the peak at the same position is also observed on the B- Fe_3O_4 @FOC surface (Fig. S16b), suggesting that the doping of B can generate a Fe-B bond [36]. The Mn $2p_{3/2}$ spectra of B- MnFe_2O_4 @MFOC and B- Mn_3O_4 @MOC are displayed in Fig. 3c and S16d, which are distinguished at ~ 641.0 and 642.8 eV, assigning to Mn^{2+} and Mn^{3+} , respectively. Similarly, a peak relating to Mn-B at ~ 637.9 eV can be fitted on either B- MnFe_2O_4 @MFOC or B- Mn_3O_4 @MOC surface. To further confirm the real oxidation state of Mn 2p, the multiplet splitting separation of Mn 3s

photopeak is fitted (Fig. S17). While, the Mn 3s spectrum splits into a doublet of peaks with a multiplet splitting energy of 6.3 eV, higher than that of Mn^{2+} (6.1 eV) [37], which indicates the real oxidation states of Mn 2p is the mixing of Mn^{2+} and Mn^{3+} . To further investigate the change of valence states after doping of B into the MnFe_2O_4 structure, a standard spinel MnFe_2O_4 sample was synthesized (Fig. S18), and the standard XPS spectrum was also fitted (Fig. S19). Comparing with the Fe 2p and Mn 2p XPS peaks of the standard MnFe_2O_4 sample, both of them for the B- MnFe_2O_4 @MFOC are shifted to a lower binding energy direction, suggesting that electron densities of the Fe and Mn should be increased due to the replacing of O with high electronegativity (3.44 of O) around the Fe and Mn elements by B with lower electronegativity (2.01 of B), which could vary the electronic structure as well as the coordination bond. Thus, B should have replaced parts of oxygen in the lattice structure of MnFe_2O_4 spinel [38]. After the doping of B into the lattice of MnFe_2O_4 spinel, the localized electrons on the B will favor the generation of higher oxidation states of Fe and Mn metals. Fig. 3e displays the B 1s spectrum of B- MnFe_2O_4 @MFOC, which can be deconvoluted into two peaks at 191.784 and 187.65 eV, assigning to the oxidized borate species and B-Metal bonds, respectively. It also indicates that B atoms could be directly bonded to metal (Fe and Mn) by the metal d-orbitals and/or the hybridization of B 2p states after NaBH_4 reduction treatment [39,40], and the binding energies of B-Fe and B-Mn for B- Fe_3O_4 @FOC and B- Mn_3O_4 @MOC are 187.42 and 187.71 eV, respectively. (Fig. S20). Herein, it should be noted that the binding energy of metal-B is higher than that of pure boron (187.0 eV), which should be beneficial for the occurrence of electron transfer from B to Fe/Mn atom. Compared with the non-metal B atom, the d-orbitals of the metal species are filled with more electrons, serving as the catalytic active sites. That is, the B atoms may not serve as the active sites directly to participate in the OER reaction but act as supplementary function to mitigate the over-oxidation of metal-sites, decrease the activation energy barrier and boost the electrocatalytic activity by donating electrons [40]. For the high-resolution O 1s spectrum of B- MnFe_2O_4 @MFOC (Fig. 3f),

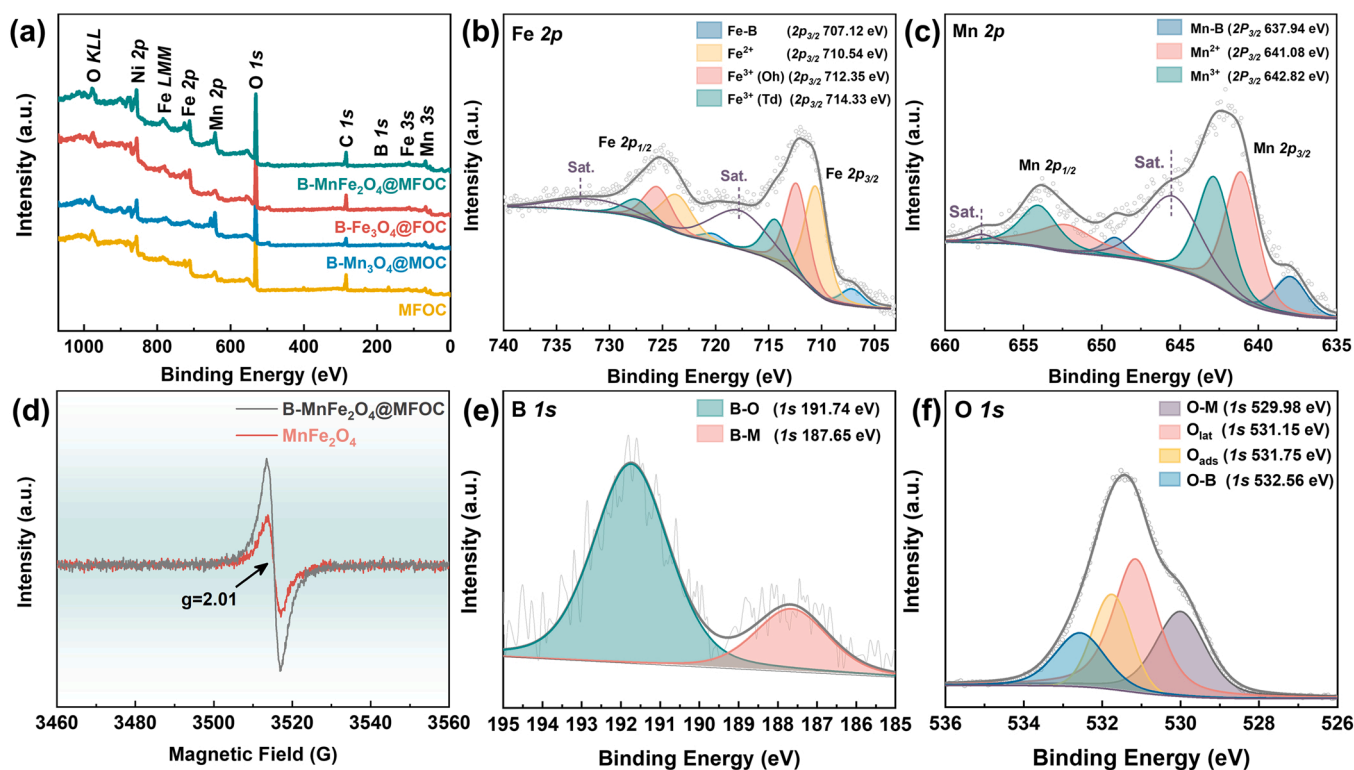


Fig. 3. (a) Full XPS profiles of B- Fe_3O_4 @FOC, B- Mn_3O_4 @MOC, MFOC and B- MnFe_2O_4 @MFOC; High-resolution XPS spectra of (b) Fe 2p; (c) Mn 2p; (e) B 1s and (f) O 1s of B- MnFe_2O_4 @MFOC; (d) EPR spectra of MnFe_2O_4 and B- MnFe_2O_4 @MFOC.

comparing with that of MFOC (Fig. S21), three peaks located at 529.98, 531.15 and 531.75 eV are assigned to the lattice O^{2-} species (O_{lat}) within the M-O bonds, adsorption oxygen (O_{ads}) from M-OH and minor chemisorbed water on the surface, respectively [41,42]. In addition, an extra peak located at 532.56 eV is observed, which should belong to the O-B bond. It should be noticed that the area of O_{ads} peak (19.13 %) is smaller than that of O_{lat} (39.4 %), suggesting that the oxygen in the oxygen-containing groups on the surface of B-MnFe₂O₄ @MFOC tends to transform into more dense lattice oxygen after the reduction [38]. Moreover, the asymmetric nature of the high energy O_{ads} demonstrates the presence of oxygen vacancy, by which it can be found that the vacancy density is increased after the NaBH₄ reduction treating. Furthermore, the oxygen vacancy density was confirmed by the electron paramagnetic resonance (EPR) measurements of B-MnFe₂O₄ @MFOC and MnFe₂O₄ [43]. As shown in Fig. 3d, there is a stronger magnetic signal at ~ 3515 G for the B-MnFe₂O₄ @MFOC, which indicates a higher concentration of unpaired electrons resulted from the oxygen defects [44]. As stated above, due to the replacing of O by B in the spinel, the electrons from the boron could be transferred to the neighboring metal sites so that the metal species such as Fe³⁺ experiences a conversion to a

more stabilized high spin state, achieving an optimal e_g filling. The corresponding overlap area of oxygen with metal ions is getting concentrated, which may cause the faster charge transfer, thereby improving the catalyst performance. It is proved by DFT calculations in the following computational section (Fig. 5).

OER linear sweep voltammetry (LSV) curves of the fabricated electrodes were assessed in 1 M KOH containing freshwater based electrolyte at first. As the preliminary experiments, various electrodes were fabricated by adjusting the molar ratio of Fe and Mn (1:10; 2:10; 3:10 and 4:10) in the initial solutions and their LSV performances were evaluated (Fig. S22). Besides, the effects of other synthesis conditions including annealing temperature (250, 350 and 450 °C) and NaBH₄ reduction time (0, 20 and 40 min) on the LSV performance were also investigated (Figs. S23 and S24). As such, it is found that the B-MnFe₂O₄ @MFOC electrocatalyst with the best OER performance should be synthesized with a Fe: Mn molar ratio of 3:10, an annealing temperature of 250 °C and NaBH₄ reduction time of 20 min, which was further studied in this work in the following.

Fig. 4a records the LSV curves without iR-corrections for the as-prepared best B-MnFe₂O₄ @MFOC, MFOC, B-Fe₃O₄ @FOC and B-

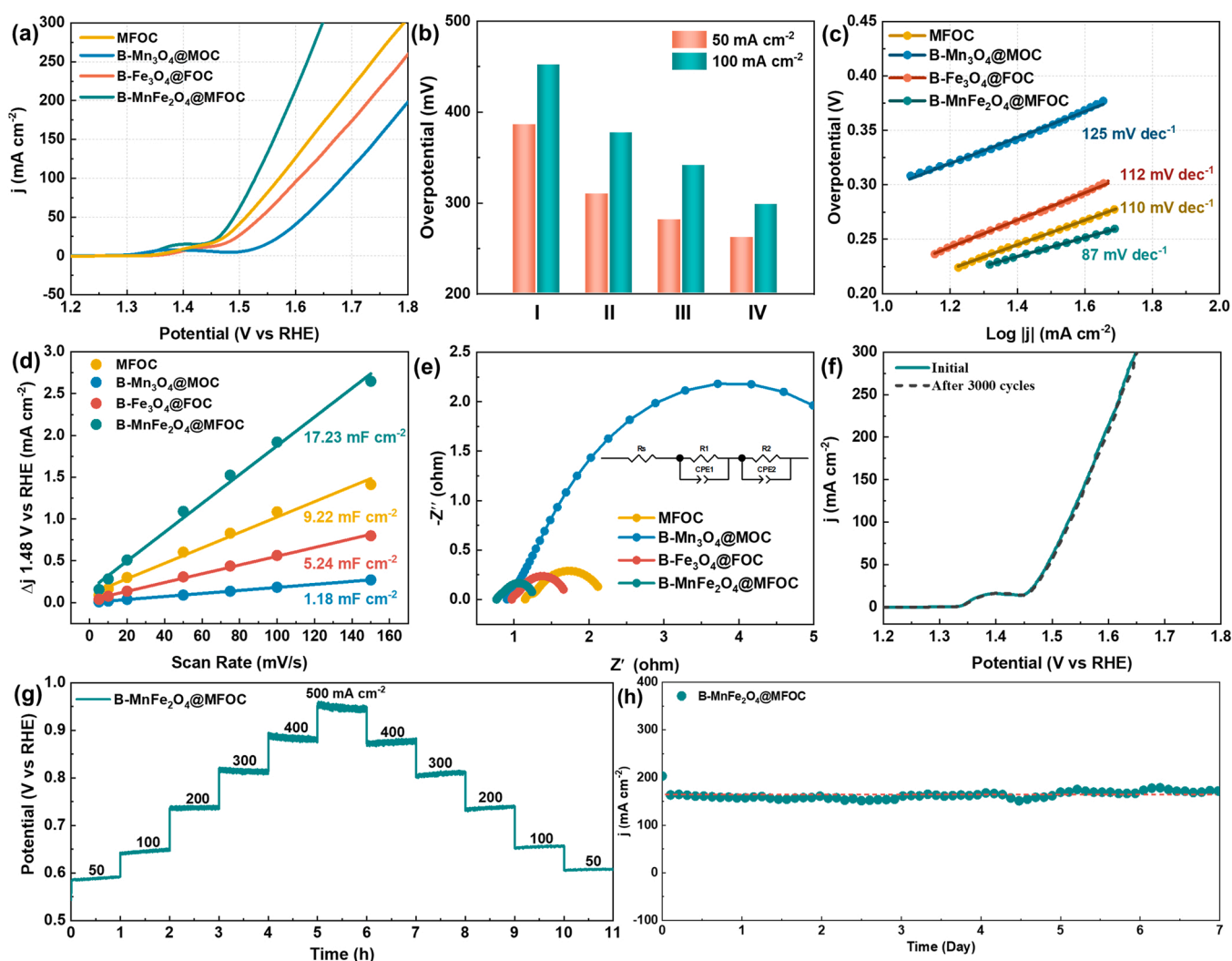


Fig. 4. OER polarization curves of B-Mn₃O₄ @MOC (I), B-Fe₃O₄ @FOC (II), MFOC (III) and B-MnFe₂O₄ @MFOC (IV) in 1 M KOH containing freshwater based electrolyte; (b) related overpotentials ($j = 50 \text{ mA cm}^{-2}$ and 100 mA cm^{-2}); (c) Tafel plots derived from the polarization curves in (a); (d) current density as a function of scan rate derived from the CV curves at different scan rates; (e) Nyquist plots and equivalent circuit model (inset); (f) polarization curves of the B-MnFe₂O₄ @MFOC electrode before and after 3000 CV cycles; (g) multi-current step test of B-MnFe₂O₄ @MFOC electrode at current densities of 50, 100, 200, 300, 400 and 500 mA cm^{-2} and (h) the chronoamperometry curves of the B-MnFe₂O₄ @MFOC electrode at the constant potential corresponding to the current density of 100 mA cm^{-2} for 7 days.

Mn₃O₄ @MOC based electrodes. Specifically, the B-MnFe₂O₄ @MFOC requires an extremely low overpotential of 298 mV at a current density of 100 mA cm⁻², which is much lower than those of MFOC (341 mV), B-Fe₃O₄ @FOC (377 mV) and B-Mn₃O₄ @MOC (452 mV) (Fig. 4b and Table S3). Meanwhile, the present B-MnFe₂O₄ @MFOC ranks the top level among those reported electrocatalysts (Table S4). While, the catalytic kinetics of the above electrocatalysts were evaluated by the Tafel slope. As shown in Fig. 4c, the Tafel slope of the B-MnFe₂O₄ @MFOC is only as low as 87 mV dec⁻¹, which is much lower than those of MFOC (110 mV dec⁻¹), B-Fe₃O₄ @FOC (112 mV dec⁻¹) and B-Mn₃O₄ @MOC (125 mV dec⁻¹), demonstrating a fastest electrocatalytic kinetics of OER. Herein, it is conjectured that the outstanding OER performance of B-MnFe₂O₄ @MFOC electrode should be mainly originated from the B-MnFe₂O₄, where MFOC possibly mainly serves as a conductor and support as discussed above since it is almost covered by the B-MnFe₂O₄. Furthermore, the electrochemical double-layer capacitances (*C_{dl}*) were evaluated based on the cyclic voltammetry curves (Fig. S25). As displayed in Fig. 4d, the *C_{dl}* of B-MnFe₂O₄ @MFOC electrode is about 17.23 mF cm⁻¹, which is significantly higher than those of MFOC (9.22 mF cm⁻¹), B-Fe₃O₄ @FOC (5.24 mF cm⁻¹) and B-Mn₃O₄ @MOC (1.18 mF cm⁻¹), indicating that the B-MnFe₂O₄ @MFOC possesses higher electrocatalytically active surface area, which may be due to that more active sites could be created by growing the spinel nanosheets. In addition, the intrinsic catalytic activity was evaluated by the overpotential required to achieve a certain density, which can be further normalized to the effective electrochemical surface area (ECSA). Fig. S26 exhibits the *j_{ECSA}*-normalized polarization curves, which indicates that the B-MnFe₂O₄ @MFOC has the highest inherent catalytic activity. The reaction kinetics and charge transfer resistance of as-prepared electrode were further explored by electrochemical impedance spectroscopy (EIS) analysis. As shown in Fig. 4e, the B-MnFe₂O₄ @MFOC electrode displays a smaller charge transfer resistance (*R_{ct}*) of 0.77 Ω than those of MFOC (0.97 Ω), B-Fe₃O₄ @FOC (1.15 Ω) and B-Mn₃O₄ @MOC (4.51 Ω) electrodes. As such, it can infer that the B-MnFe₂O₄ @MFOC should have a fast charge transfer kinetics, which accounts for its enhanced OER performance. The stability of B-MnFe₂O₄ @MFOC electrode was further tested. As shown in Fig. 4f, the current density is retained well with no obvious decrease compared to the initial one even after 3000-cycle testing. Furthermore, the multi-step chronopotentiometric curve of B-MnFe₂O₄ @MFOC electrode was measured (Fig. 4g), where the current density was changed from 50 to 500 mA cm⁻² and then returned to 50 mA cm⁻². A sharp voltage response with the current density change manifests that the composite structure has outstanding mass transport property as well as mechanical robustness for OER. Obviously, in the time interval of one hour, the potential maintains constantly under each step, indicating the excellent stability at different voltages. In addition, an electrochemical long-term stability for the B-MnFe₂O₄ @MFOC electrode was evaluated via a chrono potentiometric curve testing. As shown in Fig. 4h, a steady OER performance without obvious decrease over 7 days is achieved. Therefore, the obtained B-MnFe₂O₄ @MFOC electrode should have outstanding mechanical robustness as well as excellent catalytic stability in 1 M KOH electrolyte.

DFT calculation was employed to establish the close relationship between OER performance and electronic structure on the catalyst surface [16]. At first, the conductivities of pure carbon and Mn, Fe oxides doped into carbon species were evaluated by total density of states (DOS) calculations (Fig. S27). It is found that the metal doped carbon species has a higher DOS intensity around Fermi level, indicating that it owns superior electrical conductivity, which further proves that the MFOC in the B-MnFe₂O₄ @MFOC could provide a good conductive environment for the whole catalysts during the OER process. Then, on the basis of above characterizations, the top and side views of atomic structure models of MnFe₂O₄ and B-MnFe₂O₄ are established, in which Fe³⁺ and Mn²⁺ are coordinated with six and four oxygen atoms, respectively, and the B atom replace the O atom to bond with Fe or Mn.

(Fig. S28). After the structure optimization, it is obvious that most Fe-O bond lengths decrease significantly while Mn-O bond length basically maintains after the doping of B atom (Fig. S29 and Table S5), indicating that the doping of B atom can distort the octahedral structure, which is in agreement with the XPS analysis results as discussed above.

The effect of B introduction into MnFe₂O₄ structure was further analyzed by DOS and partial density of states (pDOS) calculations. It is found that the DOSs of both MnFe₂O₄ and B-MnFe₂O₄ are cross the Fermi level (*E_F*) (Fig. 5a-b), and the introduction of B shifts the DOS projected on Fe and Mn orbitals to near the Fermi level (Fig. S30), demonstrating that MnFe₂O₄ possesses the metallic properties in the electrical conductivity after the doping of B. From the pDOSs of MnFe₂O₄ and B-MnFe₂O₄ (Fig. 5c and d), the d orbitals of both Td sites of Mn and Oh sites of Fe overlap with the p orbitals of O, indicating that O has obvious interactions with both Mn_{Td} and Fe_{Oh}. After the O-site is substituted by B atom, the overlap area of the Fe_{Oh} with O is increased obviously, suggesting that the introduction of B atom could significantly promote the charge transfer between O and Fe_{Oh}. Moreover, compared with those in MnFe₂O₄, the orbitals of Fe d and O p centers get closer in B-MnFe₂O₄, indicating that the B-MnFe₂O₄ structure possesses greater Fe-O covalency. Herein, the larger Fe-O covalency could promote the electron transfer between metal cations and oxygen adsorbates (e.g., O₂⁻, O²⁻), thereby accelerating the OER kinetics [45]. Fig. 5e-h display the charge density distributions of MnFe₂O₄ and B-MnFe₂O₄ with top and side views, where yellow area presents positive electronic clouds accepted from others while cyan indicates the negative electronic clouds donated to others. It is clearly observed that the charge density rearrangement occurs after the introduction of B atoms. In addition, as illustrated in Fig. 5i, comparing with that of MnFe₂O₄, the band structure of B-MnFe₂O₄ is more concentrated around the Fermi level. Thus, the B-MnFe₂O₄ should have a more continuous electronic structure, expanding the range of adsorption energy, which is in agreement well with the results of DOS.

It is already identified that the OER performance of spinel type oxide is closely related to the adsorption energies of intermediates [46]. Herein, the adsorption energies of *OH, *O and *OOH species on MnFe₂O₄ and B-MnFe₂O₄ were calculated. The optimized configurations of the adsorption of intermediates on the catalytic surface during the OER process and the change of each step are presented in Fig. 5j. As a result, the rate-determine step (RDS) on the pristine MnFe₂O₄ should be the first step of the adsorption as well as the discharge of OH⁻, and the free energy (*ΔG₁*) reaches up to 5.52 eV. Surprisingly, for the B-MnFe₂O₄, the RDS seems to be the formation of *OOH since its free energy (*ΔG₃*) is as low as 2.92 eV. When *U* = 1.23 V (Fig. 5l), the reaction limiting barrier on B-MnFe₂O₄ (1.69 eV) is much lower than that on B-MnFe₂O₄ (4.92 eV). The dramatic decrease of *ΔG* indicates the enhancement of reaction kinetics, which is in good agreement with the highest intrinsic activity for B-MnFe₂O₄ in the OER process as discussed above.

Due to the high OER performance and stability for B-MnFe₂O₄ @MFOC in the 1 M KOH containing freshwater based electrolyte, whose OER performance in the seawater-based electrolyte was also evaluated. As stated in the introduction section, the most critical challenge for seawater splitting is the competition between OER and ClER at a low pH situation and chlorine oxidation reaction to generate hypochlorite at a high pH condition, which could significantly lower the efficiency of seawater oxidation. Herein, the catalytic activities of B-MnFe₂O₄ @MFOC in both alkaline simulated seawater (1 M KOH+0.5 M NaCl) and alkaline natural seawater solution (1 M KOH+ natural seawater, collected from Aomori Bay, Japan (Fig. S31)) were investigated. As shown in Fig. 6a, the B-MnFe₂O₄ @MFOC electrode requires an overpotential of 334 mV to achieve a current density of 100 mA cm⁻², which is higher than that in the freshwater based electrolyte, but much lower than those of MFOC (360 mV), B-Fe₃O₄ @FOC (414 mV) and B-Mn₃O₄ @MOC (449 mV) based electrodes. In the case using the natural seawater, as displayed in Fig. 6b, at room temperature (25 °C), the B-

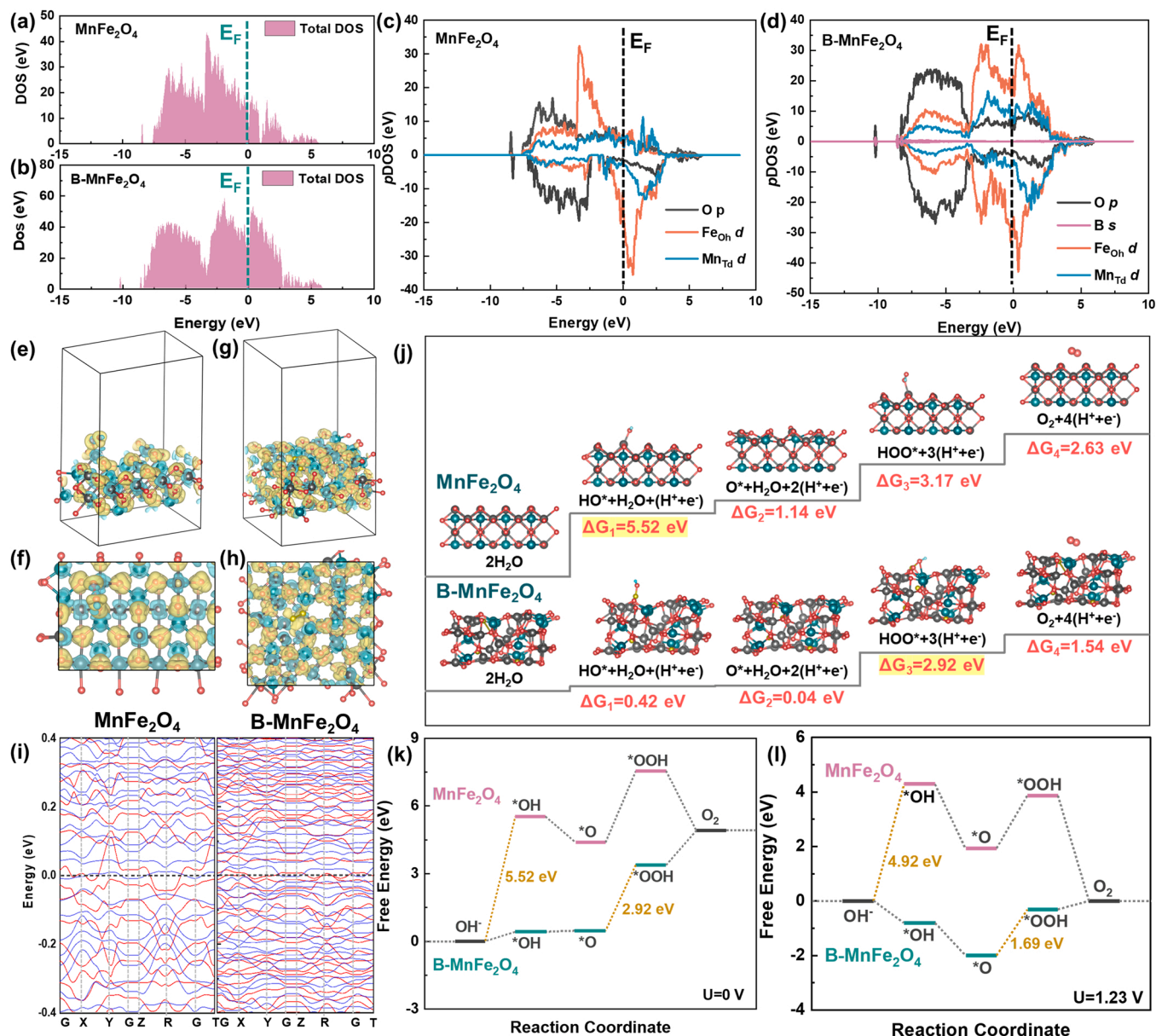


Fig. 5. Total DOSs of (a) MnFe₂O₄ and (b) B-MnFe₂O₄; pDOSs of (c) MnFe₂O₄ and (d) B-MnFe₂O₄; the charge distributions in (e-f) MnFe₂O₄ and (g-h) B-MnFe₂O₄; (i) band structures of MnFe₂O₄ and B-MnFe₂O₄; (j) the elementary steps; Gibbs free energy diagrams of MnFe₂O₄ and B-MnFe₂O₄ for OER process at (k) U = 0 V and (l) U = 1.23 V.

MnFe₂O₄ @MFOC electrode exhibits a slight decay performance with an overpotential of 405 mV at 100 mA cm⁻² when compared with the cases using freshwater and simulated seawater (Fig. 6c), which may be due to the generations of some insoluble precipitates such as Ca (OH)₂ and Mg (OH)₂ in alkaline environment, which can deposit on the electrode surface. To boost the OER activity, the electrolyte temperature was increased (Fig. 6b). As a result, the overpotentials are decreased to 380, 350 and 330 mV at 100 mA cm⁻² by heating the electrolyte to 40, 50 and 60 °C, respectively. It should be noted that such high temperatures could be easily achieved by a solar heating system on the sea. In addition, the Faradaic efficiency of B-MnFe₂O₄ @MFOC electrode for the electrolysis of 1 M KOH containing natural seawater-based electrolyte was evaluated by a drainage method. As illustrated in Fig. 6d, the measured O₂ production is matched well with the theoretical one, indicating that the Faradic efficiency is nearly 100 %, which confirms that the high OER selectivity of this B-MnFe₂O₄ @MFOC electrocatalyst in the alkaline seawater-based electrolyte.

Chloride corrosion is another tough issue in the field of seawater electrolysis since it will gradually affect the application life of a catalyst. However, the effect of chloride effect is hard to determine during the electrolysis process. In order to specifically analyze the corrosion resistance of the as-prepared electrocatalysts, the corrosion polarization curves of MFOC and B-MnFe₂O₄ @MFOC based electrodes were measured (Fig. S32), and the corresponding data are summarized in Fig. 6e. One can see that the B-MnFe₂O₄ @MFOC exhibits a higher corrosion potential (-0.616 V) and a lower corrosion current density (1.17 μA cm⁻²) than those of MFOC (-0.899 V and 1.82 μA cm⁻²), indicating that the B-MnFe₂O₄ @MFOC has higher chloride corrosion resistance ability than the MFOC. Furthermore, the durability of B-MnFe₂O₄ @MFOC in the simulated seawater and natural seawater was also determined by a two-step chron-potentiometric method sequentially at the current densities of 100 and 500 mA cm⁻². As shown in Fig. 6 f and g, no obvious voltage elevations are observed at the current densities of 100 and 500 mA cm⁻² in 100-h continuous tests,

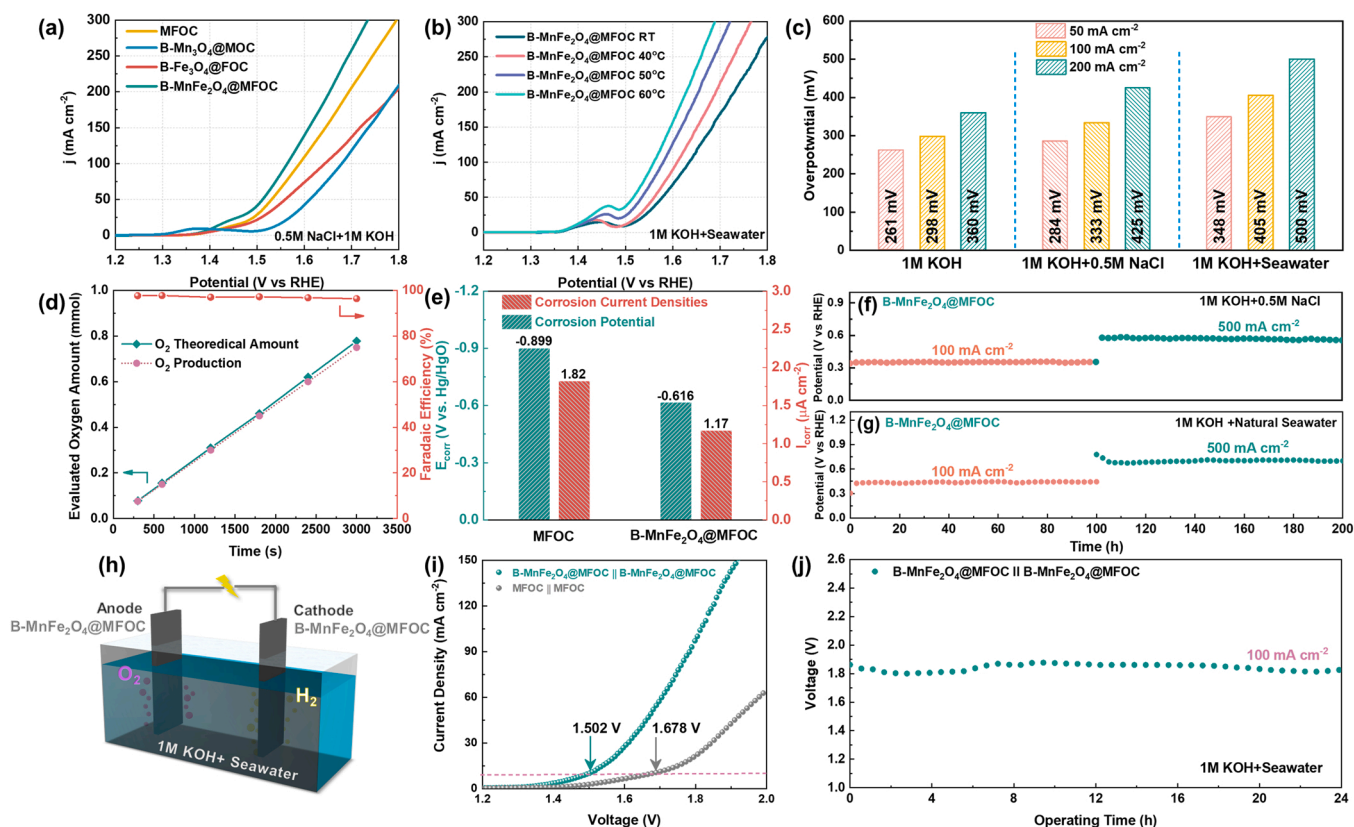


Fig. 6. OER polarization curves of as-prepared sample in (a) simulated seawater (0.5 M NaCl+1 M KOH solution) and (b) 1 M KOH+ natural seawater solution under different temperatures; (c) Comparison of the overpotentials required to achieve current densities of 50, 100 and 200 mA cm^{-2} for B-MnFe₂O₄@MFOC electrode; (d) measured and theoretical gaseous products over B-MnFe₂O₄@MFOC electrocatalyst at a current density of 100 mA cm^{-2} in 1 M KOH containing seawater based electrolyte; (e) Corrosion potentials (green) and corrosion current densities (red) of B-MnFe₂O₄@MFOC electrode in natural seawater; Chronopotentiometric curves of B-MnFe₂O₄@MFOC electrode at constant current densities of 100 and 500 mA cm^{-2} for 200 h in (f) 1 M KOH+ 0.5 M NaCl and (g) 1 M KOH+ seawater; (h) Schematic illustration of a seawater-splitting electrolyzer using B-MnFe₂O₄@MFOC for both electrodes; (i) Overall seawater splitting performance of MFOC||MFOC and B-MnFe₂O₄@MFOC||B-MnFe₂O₄@MFOC couples in 1 M KOH+ natural seawater; (j) Chronopotentiometric curves at 100 mA cm^{-2} for 24 h.

demonstrating the outstanding durability of B-MnFe₂O₄@MFOC under a high current density in both simulated seawater- and natural seawater-based electrolytes. The changes of component and structure of B-MnFe₂O₄@MFOC after the OER stability test in seawater-based electrolyte were also characterized by TEM and XPS analyses. As illustrated in Figs. S33 a-c, the morphology of nanosheet@ nanowire heterostructure has no obvious change, and the overall hierarchical nanosheet@ nanowire structure also maintains in the micro scale. Furthermore, the fringe lattice spacings of 0.295 and 0.297 nm are indexed clearly, both of which are consistent with the interplanar distances of spinel MnFe₂O₄ (220) plane, which confirms the outstanding chlorine corrosion resistance of the B-MnFe₂O₄@MFOC catalyst. In addition, EDS-mappings also indicate the existence of boron element in the spent catalyst. While, the XPS spectra of B-MnFe₂O₄@MFOC after the OER stability test (Fig. S34) show that the peaks of Fe 2p and Mn 2p remain unchanged after the OER test, demonstrating that the crystalline MnFe₂O₄ is relatively stable during seawater oxidation. Also, the specific peak of B is still maintained, indicating that more boron atoms have been doped into MnFe₂O₄ crystalline to form a metallic boride than the existence on the surface.

HER performances of the B-MnFe₂O₄@MFOC composite and MFOC were also tested in natural seawater (Fig. S35). As a result, the η_{10} values of 64 and 210 mV are required with Tafel slopes of 77 and 150 mV dec^{-1} for B-MnFe₂O₄@MFOC and MFOC, respectively. Due to the outstanding OER and HER activities of B-MnFe₂O₄@MFOC composite, the overall alkaline seawater splitting performance was investigated by integrating it as the bifunctional electrocatalyst on both anode and cathode into a two-electrode electrolyzer, as illustrated in Fig. 6 h. Consequently, the

B-MnFe₂O₄@MFOC||B-MnFe₂O₄@MFOC and MFOC||MFOC cell voltages required to achieve a current density of 10 mA cm^{-2} are 1.502 and 1.678 V, respectively, in the natural seawater-based electrolyte (Fig. 6i). It should be noticed that the B-MnFe₂O₄@MFOC||B-MnFe₂O₄@MFOC is superior to the most of the recent reported electrocatalysts based cells, which can be seen in Table S6. More importantly, the electrolyzer retains the outstanding durability with no obvious degradation over 24-h chronopotentiometry operation at a current density of 100 mA cm^{-2} (Fig. 6j). In addition, the possible generation of Cl⁻ oxidation products (e.g., ClO⁻) during seawater splitting is measured by the iodometric titrations method. As shown in Fig. S36, no obvious pink color in the solution, clearly indicating the absence of any hypochlorite trace, which further confirms the high OER selectivity in the tested system.

4. Conclusion

In summary, we have successfully synthesized an electrocatalyst with a nanocrystalline boron doped MnFe₂O₄ spinel shell covering on an amorphous MFOC core (B-MnFe₂O₄@MFOC) at room temperature using a reduction-crystallization method. The hierarchical nanosheet@ nanowire structure and hydrophilic feature make it possess favorable synergistic effect for the seawater splitting. It is found that the boron-doped MnFe₂O₄ can induce the formation of oxygen vacancies and significantly promote the charge transfer between O and Fe_{OH}. As a result, the optimum B-MnFe₂O₄@MFOC electrocatalyst exhibits a superior OER activity with an overpotential as low as 298 mV cm^{-2} at 100 mA cm^{-2} and a long-term stability over 7 days in freshwater-based electrolyte. Meanwhile, it also shows an excellent OER performance and

high corrosion-resistance in the alkaline natural seawater. This work provides a facile method to prepare electrocatalysts suitable for different electrolytes with high stability in the seawater splitting process.

CRediT authorship contribution statement

Meng Chen: Conceptualization, Methodology, Formal analysis, Investigation, Writing – original draft. **Nutthaphak Kitiphatpiboon:** Investigation. **Changrui Feng:** Investigation. **Qiang Zhao:** Investigation. **Abuliti Abudula:** Investigation. **Yufei Ma:** Conceptualization, Methodology, Supervision, Validation, Writing – review & editing. **Kai Yan:** Software, Supervision, Validation, Writing – review & editing. **Guoqing Guan:** Conceptualization, Methodology, Project administration, Funding acquisition, Resources, Supervision, Validation, Writing – review & editing.

Declaration of Competing Interest

The authors declare that they have no known competing financial interests or personal relationships that could have appeared to influence the work reported in this paper.

Data availability

Data will be made available on request.

Acknowledgements

This work is supported by ZiQoo Chemical Co. Ltd., Japan, Hirosaki University Fund and Hydrogen Energy Systems Society of Japan. The authors acknowledge Shared Facility Center for Science and Technology (SFCST), Hirosaki University, Japan, for TEM-EDX, XRD and SEM-EDX measurements. Chen and Feng gratefully acknowledge the State Scholarship Fund of China Scholarship Council, China. Kitiphatpiboon gratefully acknowledges MEXT of Japan for the scholarship, Japan. We acknowledge computational resources provided by Hefei advanced computing center. The authors also thanks Dr. Ping Wu for discussion of DFT and computational analysis.

Appendix A. Supporting information

Supplementary data associated with this article can be found in the online version at [doi:10.1016/j.apcatb.2023.122577](https://doi.org/10.1016/j.apcatb.2023.122577).

References

- [1] L. Li, G. Zhang, B. Wang, S. Yang, Constructing the Fe/Cr double (oxy)hydroxides on Fe₃O₄ for boosting the electrochemical oxygen evolution in alkaline seawater and domestic sewage, *Appl. Catal. B Environ.* 302 (2022), 120847.
- [2] H. Zhang, D. Guan, Z. Hu, Y.C. Huang, X. Wu, J. Dai, C.L. Dong, X. Xu, H.J. Lin, C. T. Chen, W. Zhou, Z. Shao, Exceptional lattice-oxygen participation on artificially controllable electrochemistry-induced crystalline-amorphous phase to boost oxygen-evolving performance, *Appl. Catal. B Environ.* 297 (2021), 120484.
- [3] Z. Feng, E. Wang, S. Huang, J. Liu, A bifunctional nanoporous Ni-Co-Se electrocatalyst with a supraerophobic surface for water and hydrazine oxidation, *Nanoscale* 12 (2020) 4426–4434.
- [4] K. Deng, Q. Mao, W. Wang, P. Wang, Z. Wang, Y. Xu, X. Li, H. Wang, L. Wang, Defect-rich low-crystalline Rh metallene for efficient chlorine-free H₂ production by hydrazine-assisted seawater splitting, *Appl. Catal. B Environ.* 310 (2022), 121338.
- [5] Z. Feng, T. Shi, W. Liu, W. Zhang, H. Zhang, Highly active bifunctional electrocatalyst: nanoporous (Ni, Co)_{0.85}Se anchored on rGO for water and hydrazine oxidation, *Int. J. Energy Res.* 46 (2022) 15938–15947.
- [6] W. Liu, T. Shi, Z. Feng, Bifunctional zeolitic imidazolate framework-67 coupling with CoNiSe electrocatalyst for efficient hydrazine-assisted water splitting, *J. Colloid Interf. Sci.* 630 (2023) 888–899.
- [7] J. Li, G. Zheng, One-dimensional earth-abundant nanomaterials for water-splitting electrocatalysts, *Adv. Sci.* 4 (2017) 1600380.
- [8] X. Xiao, L. Yang, W. Sun, Y. Chen, H. Yu, K. Li, B. Jia, L. Zhang, T. Ma, Electrocatalytic water splitting: from harsh and mild conditions to natural seawater, *Small* 18 (2022) 2105830.
- [9] J. Liu, X. Liu, H. Shi, J. Luo, L. Wang, J. Liang, S. Li, L.M. Yang, T. Wang, Y. Huang, Q. Li, Breaking the scaling relations of oxygen evolution reaction on amorphous NiFeP nanostructures with enhanced activity for overall seawater splitting, *Appl. Catal. B Environ.* 302 (2022), 120862.
- [10] C. Wang, H. Shang, L. Jin, H. Xu, Y. Du, Advances in hydrogen production from electrocatalytic seawater splitting, *Nanoscale* 13 (2021) 7897–7912.
- [11] B. Cui, Z. Hu, C. Liu, S. Liu, F. Chen, S. Hu, J. Zhang, W. Zhou, Y. Deng, Z. Qin, Z. Wu, Y. Chen, L. Cui, W. Hu, Heterogeneous lamellar-edged Fe-Ni (OH)₂/Ni₃S₂ nanoribbon for efficient and stable seawater oxidation, *Nano Res.* 14 (2021) 1149–1155.
- [12] K.S. Exner, J. Anton, T. Jacob, H. Over, Full kinetics from first principles of the chlorine evolution reaction over a RuO₂ (110) model electrode, *Angew. Chem. Int. Ed.* 55 (2016) 7501–7504.
- [13] J. Liu, S. Duan, H. Shi, T. Wang, X. Yang, Y. Huang, G. Wu, Q. Li, Rationally designing efficient electrocatalysts for direct seawater splitting: challenges, achievements, and Promises, *Angew. Chem. Int. Ed.* (2022) 202210753.
- [14] H.Y. Wang, C.C. Weng, J.T. Ren, Z.Y. Yuan, An overview and recent advances in electrocatalysts for direct seawater splitting, *Front. Chem. Sci. Eng.* 15 (2021) 1408–1426.
- [15] Q. Zhao, Z. Yan, C. Chen, J. Chen, Spinel: controlled Preparation, Oxygen reduction/evolution reaction application, and beyond, *Chem. Rev.* 117 (2017) 10121–10211.
- [16] J. Sun, N. Guo, Z. Shao, K. Huang, Y. Li, F. He, Q. Wang, A facile strategy to construct amorphous spinel-based electrocatalysts with massive oxygen vacancies using ionic liquid dopant, *Adv. Energy Mater.* 8 (2018) 1800980.
- [17] L. Xu, Q. Jiang, Z. Xiao, X. Li, J. Huo, S. Wang, L. Dai, Plasma-engraved Co₃O₄ nanosheets with oxygen vacancies and high surface area for the oxygen evolution reaction, *Angew. Chem. Int. Ed.* 128 (2016) 5363–5367.
- [18] D. Wang, Y. Chen, L. Fan, T. Xiao, T. Meng, Z. Xing, X. Yang, Bulk and surface dual modification of nickel-cobalt spinel with ruthenium toward highly efficient overall water splitting, *Appl. Catal. B Environ.* 305 (2022), 121081.
- [19] S. Chen, D. Huang, D. Liu, H. Sun, W. Yan, J. Wang, M. Dong, X. Tong, W. Fan, Hollow and porous NiCo₂O₄ nanospheres for enhanced methanol oxidation reaction and oxygen reduction reaction by oxygen vacancies engineering, *Appl. Catal. B Environ.* 291 (2021), 120065.
- [20] C. Mu, J. Mao, J. Guo, Q. Guo, Z. Li, W. Qin, Z. Hu, K. Davey, T. Ling, S. Qiao, Rational design of spinel cobalt vanadate oxide Co₂VO₄ for superior electrocatalysis, *Adv. Mater.* 32 (2020) 1907168.
- [21] S. Deng, Z. Tie, F. Yue, H. Cao, M. Yao, Z. Niu, Rational design of ZnMn₂O₄ quantum dots in a carbon framework for durable aqueous Zinc-ion batteries, *Angew. Chem. Int. Ed.* 134 (2022), e202115877.
- [22] C. Wei, Z. Feng, G.G. Scherer, J. Barber, Y. Shao-Horn, Z.J. Xu, Cations in octahedral sites: a descriptor for oxygen electrocatalysis on transition-metal spinels, *Adv. Mater.* 29 (2017) 1606800.
- [23] J. Zhang, X. Shang, H. Ren, J. Chi, H. Fu, B. Dong, C. Liu, Y. Chai, Modulation of inverse spinel Fe₃O₄ by phosphorus doping as an industrially promising electrocatalyst for hydrogen evolution, *Adv. Mater.* 31 (2019), 1905107.
- [24] W. Xie, J. Huang, L. Huang, S. Geng, S. Song, P. Tsiakaras, Y. Wang, Novel fluorine-doped cobalt molybdate nanosheets with enriched oxygen-vacancies for improved oxygen evolution reaction activity, *Appl. Catal. B Environ.* 303 (2022), 120871.
- [25] D.K. Bediako, Y. Surendranath, D.G. Nocera, Mechanistic studies of the oxygen evolution reaction mediated by a nickel-borate thin film electrocatalyst, *J. Am. Chem. Soc.* 135 (2013) 3662–3674.
- [26] M. Yu, C. Weidenthaler, Y. Wang, E. Budiyo, E. Onur Sahin, M. Chen, S. DeBeer, O. Rüdiger, H. Tüysüz, Surface boron modulation on cobalt oxide nanocrystals for electrochemical oxygen evolution reaction, *Angew. Chem. Int. Ed.* 61 (2022), e202211543.
- [27] N. Wen, Y. Xia, H. Wang, D. Zhang, H. Wang, X. Wang, X. Jiao, D. Chen, Large-scale synthesis of spinel Ni_{0.5}Mn_{1.5}O₄ solid solution immobilized with iridium single atoms for efficient alkaline seawater electrolysis, *Adv. Sci.* 9 (2022) 2200529.
- [28] L. Bigiani, D. Barreca, A. Gasparotto, T. Andreu, J. Verbeeck, C. Sada, E. Modin, O. I. Lebedev, J.R. Morante, C. Maccato, Selective anodes for seawater splitting via functionalization of manganese oxides by a plasma-assisted process, *Appl. Catal. B Environ.* 284 (2021), 119684.
- [29] L. Wu, L. Yu, Q. Zhu, B. McElhenny, F. Zhang, C. Wu, X. Xing, J. Bao, S. Chen, Z. Ren, Boron-modified cobalt iron layered double hydroxides for high efficiency seawater oxidation, *Nano Energy* 83 (2021), 105838.
- [30] F. Cheng, J. Shen, B. Peng, Y. Pan, Z. Tao, J. Chen, Rapid room-temperature synthesis of nanocrystalline spinels as oxygen reduction and evolution electrocatalysts, *Nat. Chem.* 3 (2011) 79–84.
- [31] M. Rinawati, Y.X. Wang, K.Y. Chen, M.H. Yeh, Designing a spontaneously deriving NiFe-LDH from bimetallic MOF-74 as an electrocatalyst for oxygen evolution reaction in alkaline solution, *Chem. Eng. J.* 423 (2021), 130204.
- [32] A. Sivakumar, S. Sahaya Jude Dhas, P. Sivaprakash, A.I. Almansour, R. Suresh Kumar, N. Arumugam, K. Perumal, S. Arumugam, S.A. Martin, Britto Dhas, Raman spectroscopic and electrochemical measurements of dynamic shocked MnFe₂O₄ nano-crystalline materials, *J. Inorg. Organomet. Polym.* 32 (2022) 344–352.
- [33] W. Wang, Z. Ding, X. Zhao, S. Wu, F. Li, M. Yue, J.P. Liu, Microstructure and magnetic properties of MFe₂O₄ (M = Co, Ni, and Mn) ferrite nanocrystals prepared using colloidal mill and hydrothermal method, *J. Appl. Phys.* 117 (2015) 17A328.
- [34] P. Bandyopadhyay, G. Saeed, N.H. Kim, J.H. Lee, Zinc-nickel-cobalt oxide@NiMoO₄ core-shell nanowire/nanosheet arrays for solid state asymmetric supercapacitors, *Chem. Eng. J.* 384 (2020), 123357.
- [35] M.S. Matseke, H. Zheng, M.K. Mathe, E. Carleschi, B. Doyle, Influence of Co doping on physiochemical properties of MnFe₂O₄/C nano compounds toward oxygen reduction reaction, *J. Alloy. Compd.* 888 (2021), 161581.

- [36] J. Masa, P. Weide, D. Peeters, I. Sinev, W. Xia, Z. Sun, C. Somsen, M. Muhler, W. Schuhmann, Amorphous cobalt boride (Co₂B) as a highly efficient nonprecious catalyst for electrochemical water splitting: oxygen and hydrogen evolution, *Adv. Energy Mater.* 6 (2016), 1502313.
- [37] X. Zhao, X. Li, Y. Yan, Y. Xing, S. Lu, L. Zhao, S. Zhou, Z. Peng, J. Zeng, Electrical and structural engineering of cobalt selenide nanosheets by Mn modulation for efficient oxygen evolution, *Appl. Catal. B* 236 (2018) 569–575.
- [38] L. Han, B. Li, S. Tao, J. An, B. Fu, Y. Han, W. Li, X. Li, S. Peng, T. Yin, Graphene oxide-induced formation of a boron-doped iron oxide shell on the surface of NZVI for enhancing nitrate removal, *Chemosphere* 252 (2020), 126496.
- [39] Q. Li, L. Lina, X. Ai, H. Chen, J. Zou, G.D. Li, X. Zou, Multiple crystal phases of intermetallic tungsten borides and phasedependent electrocatalytic property for hydrogen evolution, *Chem. Commun.* 56 (2020) 13983–13986.
- [40] Y. Wang, D. Jia, W. Zhang, G. Jia, H. Xie, W. Ye, G. Zhu, P. Gao, A boronization-induced amorphous-crystalline interface on a Prussian blue analogue for efficient and stable seawater splitting, *Chem. Commun.* 58 (2022) 6132–6135.
- [41] M.S. Matseke, H. Zheng, Y. Wang, The ultrasonication boosts the surface properties of CoFe₂O₄/C nanoparticles towards ORR in alkaline media, *Appl. Surf. Sci.* 516 (2020), 146105.
- [42] M. Fang, D. Han, W. Xu, Y. Shen, Y. Lu, P. Cao, S. Han, W. Xu, D. Zhu, W. Liu, J. C. Ho, Surface-guided formation of amorphous mixed-metal oxyhydroxides on ultrathin MnO₂ nanosheet arrays for efficient electrocatalytic oxygen evolution, *Adv. Energy Mater.* 10 (2020), 2001059.
- [43] Y. Li, J. Chen, P. Cai, Z. Wen, An electrochemically neutralized energy-assisted low-cost acid-alkaline electrolyzer for energy-saving electrolysis hydrogen generation, *J. Mater. Chem. A* 6 (2018) 4948–4954.
- [44] S. Sun, T. Zhai, C. Liang, S.V. Savilov, H. Xia, Boosted crystalline/amorphous Fe₂O_{3-δ} core/shell heterostructure for flexible solid-state pseudocapacitors in large scale, *Nano Energy* 45 (2018) 390–397.
- [45] Y. Zhou, S. Sun, J. Song, S. Xi, B. Chen, Y. Du, A.C. Fisher, F. Cheng, X. Wang, H. Zhang, Z.J. Xu, Enlarged Co-O covalency in octahedral sites leading to highly efficient spinel oxides for oxygen evolution reaction, *Adv. Mater.* 30 (2018), 1802912.
- [46] J.S. Kim, B. Kim, H. Kim, K. Kang, Recent progress on multimetal oxide catalysts for the oxygen evolution reaction, *Adv. Energy Mater.* 8 (2018), 1702774.